Chinese Chemical Letters 35 (2024) 108899

Contents lists available at ScienceDirect

Chinese Chemical Letters

journal homepage: www.elsevier.com/locate/cclet

Efficient production of ligand-free microscintillators at gram-scale for high-resolution X-ray luminescence imaging

Hao Jiang[a], Qihao Chen[a,c], Hongyu Wang[a,c], Tingting Wu[a], Jianwei Gong[a], Zhenzhen Zhang[a,d,*], Qiushui Chen[a], Huanghao Yang[a,*], Lili Xie[b,*]

[a] New Cornerstone Science Laboratory, MOE Key Laboratory for Analytical Science of Food Safety and Biology, College of Chemistry, Fuzhou University, Fuzhou 350108, China
[b] School of Public Health, Fujian Medical University, Fuzhou 350108, China
[c] Joint School of National University of Singapore and Tianjin University, Fuzhou International Campus of Tianjin University, Fuzhou 350207, China
[d] Beijing National Laboratory for Molecular Sciences, College of Chemistry and Molecular Engineering, Peking University, Beijing 100871, China

ARTICLE INFO

Article history:
Received 26 April 2023
Revised 17 July 2023
Accepted 5 August 2023
Available online 6 August 2023

Keywords:
Microscintillators
$NaLuF_4$:Tb^{3+}
Afterglow
X-ray detector
X-ray luminescence imaging

ABSTRACT

The efficient production of high-quality scintillators with long radioluminescence afterglow is crucial for high-performance X-ray luminescence extension imaging. However, scaling-up the synthesis of ligand-free scintillators to fabricate large-area X-ray imaging screens for industrial applications remains a challenge. In this study, we report an efficient method to synthesize ligand-free, lanthanide-doped microscintillators by a one-pot reaction *via* the concentrated hydrothermal method. The as-synthesized microscintillators exhibit prolonged persistent radioluminescence for up to 30 days after X-ray exposure and remain high stability in air or water for more than 18 months without deterioration. Monte Carlo simulations indicate that the size effect is responsible for the excellent afterglow performance of the microscintillators. We employ these high-quality lanthanide-doped microscintillators to fabricate a large-area X-ray imaging detector using a blade-coating method, a spatial resolution of 24.9 lp/mm for X-ray imaging. Our study offers a solution for scaling-up the synthesis of low-cost microscintillators for practical applications.

X-ray imaging is widely used in various fields, including biomedicine [1–3], non-destructive detection [4–6], and national defense security [7–9]. Scintillators, which produce light when they absorb radiation [10,11], are crucial in certain types of X-ray detection and imaging. However, conventional scintillators such as $CaWO_4$, CsI:Tl, and Gd_2O_2S:Tb are usually grown by a solid-state method at high temperatures, making them expensive and difficult to fabricate into large-area scintillator films [12,13]. In recent years, solution-processed scintillators synthesized at relatively low temperatures, such as perovskites, metal-organic frameworks (MOFs), and atomically precise metal nanoclusters, have emerged as next-generation candidates for low-cost X-ray sensing [14–18]. For example, solution-processed perovskite nanocrystal scintillators have demonstrated high sensitivity to X-ray irradiation, making it possible to fabricate low-dose, large-area, and flexible X-ray detectors [19,20]. High-Z MOF nanocrystals have shown an ultrafast scintillation rise time of ~50 ps upon X-ray irradiation, offering the opportunity to achieve high-resolution imaging [21,22]. Despite their promising performance, current scintillators require integration with silicon-based photodetectors to achieve in-time readout of radioluminescence for indirect X-ray detection [23].

Recently, lanthanide-doped fluoride nanoscintillators have demonstrated the ability to harvest X-ray energies and generate high-efficiency radioluminescence, owing to their low phonon vibrational energy (<350 cm^{-1}) and reduced non-radiative relaxation transitions [24,25]. One particularly intriguing development is the creation of lanthanide-doped fluoride nanoscintillators with long-lasting radioluminescence afterglow for flexible X-ray imaging [26–28]. This unique property of the lanthanide-doped fluoride nanoscintillators is well-suited for achieving X-ray irradiation memory and information storage, making them appealing for developing flat-panel-free, flexible X-ray detectors [29,30]. However, these lanthanide-doped nanocrystal scintillators are typically synthesized by an oily ligand-mediated coprecipitation method, which presents a challenge for scaling up synthesis and large-area fabrication, and thus may impede industrialization [31].

Here we report a facile strategy to achieve large-scale synthesis of ligand-free microscintillators using a hydrothermal method. Our method can yield high-quality $NaLuF_4$:Tb^{3+} microscintillators

* Corresponding authors.
E-mail addresses: zhenzhenzhang@fzu.edu.cn (Z. Zhang), hhyang@fzu.edu.cn (H. Yang), 1006xielili@fjmu.edu.cn (L. Xie).

https://doi.org/10.1016/j.cclet.2023.108899
1001-8417/

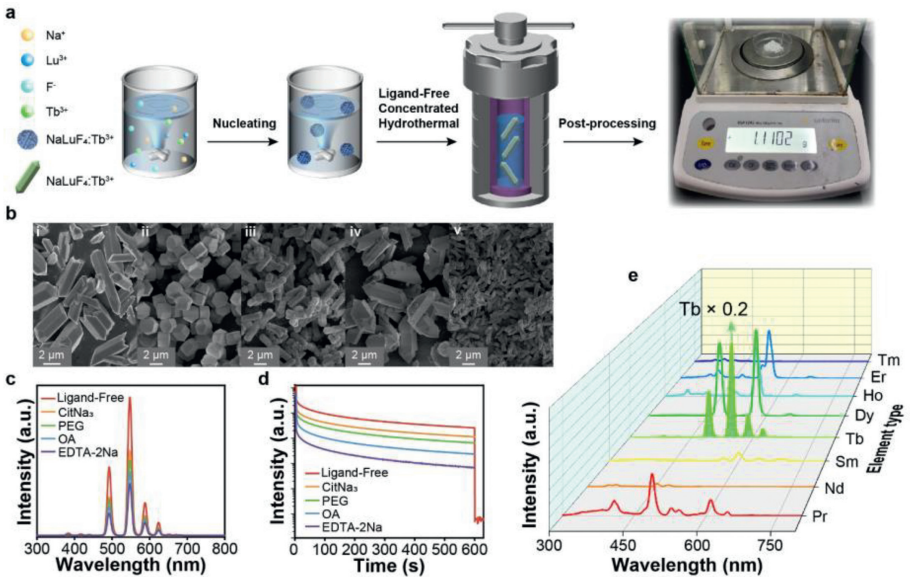

Fig. 1. Synthesis and characterization of lanthanide-doped scintillators. (a) Schematic procedure for large-scale synthesis of $NaReF_4:Ln^{3+}$ *via* a concentrated hydrothermal method. (b) Scanning electron microscopy (SEM) images of $NaLuF_4:Tb^{3+}$ without organic ligands (i), and with organic ligands of $CitNa_3$ (ii), EDTA-2Na (iii), PEG (iv), and OA (v). (c) Emission spectra of $NaLuF_4:Tb^{3+}$ with ligand-free, $CitNa_3$, PEG, OA, and EDTA-2Na as ligands respectively. (d) Comparison of radioluminescence afterglow decay profiles of various microscintillators after cessation of X-ray excitation (wavelength = 547 nm, 50 kV). (e) Emission spectra of $NaLuF_4$ doped with different activator ions (Tm^{3+}, Er^{3+}, Ho^{3+}, Dy^{3+}, Tb^{3+}, Sm^{3+}, Nd^{3+}, Pr^{3+}).

at gram-scale in a single reaction. These microscintillators exhibit an ultralong radioluminescence of up to 30 days after X-ray irradiation. We have also developed a blade-coating method to incorporate these long afterglow microscintillators with flexible PDMS substrates to fabricate large-area X-ray detectors. These detectors demonstrate high sensitivity in response to X-ray exposure and high spatial resolution for X-ray imaging. Our experimental results also demonstrate that these X-ray detectors can store information for more than a month with high-quality X-ray luminescence imaging.

In a typical experiment, we synthesized $NaLuF_4:Tb^{3+}$ scintillators with controlled morphologies from nanometer to microscale using a concentrated hydrothermal method (Figs. 1a and b, Fig. S1 in Supporting information). Gram-scale microscintillators were easily produced from a single hydrothermal reaction through compressing the concentration of the reactants and discarding the use of ligands. It is importantly found that such ligand-free reaction greatly expanded the yield per unit volume and also enhanced the radioluminescent properties of the scintillators. As shown in Figs. 1c and d, the radioluminescence properties of the ligand-free scintillators were 66% higher than those of the scintillators using sodium citrate as the ligand, and the radioluminescence afterglow intensities were 128% higher. We reason that this enhancement was attributed to both the energy dissipation by the vibration of hydroxyl radicals on the ligands and size effect of scintillator particles. Fig. 1b showed that the morphologies of the lanthanide-doped fluoride scintillators were controlled by changing different ligands, because the orientation of crystal growth was governed by the ligands [32]. Additionally, by adjusting the doping concentration of Tb^{3+} activators and the ratio of nucleating agent sodium fluoride (NaF) and ammonium fluoride (NH_4F), we determined that the optimal doping concentration of Tb^{3+} ions was 20% and the ratio of NaF and NH_4F is 1:4 (Figs. S2–S4 in Supporting information). The XRD patterns of $NaLuF_4:Tb^{3+}$ scintillators with different Tb^{3+} concentrations and the ratio of nucleating agents indicated that the crystalline phases of all the samples match well with the standard card of the hexagonal-phase $NaLuF_4$ (JCPDS card No. 27–0726) (Fig. S5 in Supporting information). Moreover, scintillators from nanometer to microscale were synthesized by varying the time, temperature, and alkali content (Figs. S6–S9 in Supporting information). Similarly, $NaLuF_4:Ln^{3+}$ ($Ln^{3+} = Tm^{3+}$, Er^{3+}, Ho^{3+}, Dy^{3+}, Sm^{3+}, Nd^{3+}, Pr^{3+}) were readily synthesized via the ligand-free concentrated hydrothermal method, which indicates the versatility of the strategy developed in this study (Fig. 1e and Fig. S1).

We next examined the photophysical properties of the as-prepared $NaLuF_4$: Tb^{3+} microscintillators. As shown in Fig. 2a, we compared the absorption coefficient of the $NaLuF_4$, $NaGdF_4$, and $NaYF_4$ with commercial scintillators GOS and CsI:Tl in the range of 1–1000 keV, and found that $NaLuF_4$ was more suitable for use as a host. It is worth noting that the heavy atom effect is very significant for the X-ray absorption and scintillation. Accordingly, we observed that the as-synthesized $NaLuF_4:Tb^{3+}$ had the best X-ray-excited luminescence and afterglow duration (Fig. S10 in Supporting information). The $NaLuF_4:Tb^{3+}$ exhibited a very obvious X-ray charging property and strong radioluminescence afterglow (Fig. 2b). By doping with various lanthanide ions (Tm^{3+}, Er^{3+}, Ho^{3+}, Dy^{3+}, Tb^{3+}, Sm^{3+}, Nd^{3+}, Pr^{3+}), the radioluminescence of the as-synthesized scintillators were tunable, as indicated in the CIE chromaticity coordinate diagram (Fig. 2c). We demonstrated that the radioluminescence intensity of the $NaLuF_4:Tb^{3+}$ exhibited a broad linear range with the X-ray dose rate of 1–278 μGy/s (Fig. 2d). It was also found that the radioluminescence intensity was sufficiently stable even under a high dose rate (278 μGy/s) of repeated X-ray excitation for 165 on-off cycles and 300 s of continuous daily irradiation for 5 days (Fig. 2e). Meanwhile, the $NaLuF_4:Tb^{3+}$ microscintillators had outstanding photostability on both radioluminescence and persistent luminescence against continuous irradiation at high dose rates and even being stored in air and water for up to 18 months (Fig. 2f and Fig. S11 in Supporting information). Notably, the ligand-free microscintillators emitted ultralong radioluminescence afterglow at time intervals from 0 to 21 days upon switching off the X-ray source (60 kV, 0.2 mA), which was also still detectable after 300 days of storage at room temperature upon heating at 120 °C (Fig. 2g). These experimental observations

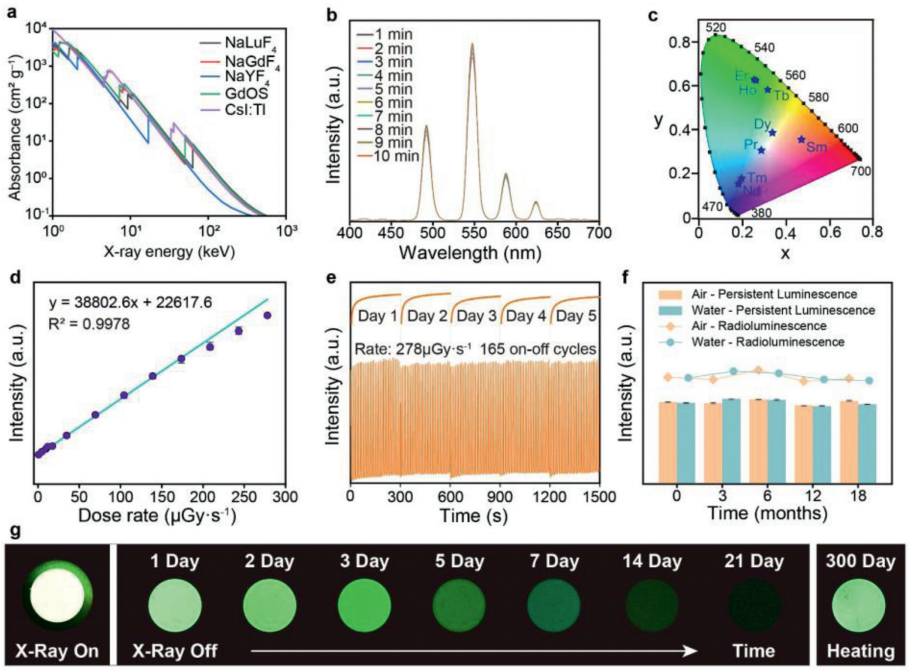

Fig. 2. Optical investigation of ligand-free $NaLuF_4:Tb^{3+}$ microscintillators. (a) Absorption spectra of $NaLuF_4$, $NaGdF_4$, $NaYF_4$, GOS and CsI:Tl as a function of X-ray energy. Attenuation coefficients were obtained from Ref. [33]. (b) Emission spectra of $NaLuF_4:Tb^{3+}$ microscintillators with increasing excitation time. (c) CIE (Commission Internationale de l'Eclairage) chromaticity coordinates of radioluminescence color of $NaLuF_4$ doped with different activator ions. (d) Radioluminescence measurements for $NaLuF_4:Tb^{3+}$ microscintillators as a function of dose rate. All measurements were performed three times. (e) Photostability of $NaLuF_4:Tb^{3+}$ microscintillators against continuous X-ray irradiation and repeated cycles of X-ray excitation with a 3-second X-ray excitation and a 6-second stop X-ray excitation interval (wavelength = 547 nm, 50 kV). (f) Stability of the as-synthesized microscintillators in air and water after 18 months of storage. (g) Radioluminescence afterglow photographs of $NaLuF_4:Tb^{3+}$ microscintillators powders, recorded with a CMOS camera at time intervals from 0 to 21 days (60 kV, 0.2 mA), and thermoluminescence photo at 120 °C after 300 days.

demonstrated the outstanding X-ray memory capability of the as-synthesized ligand-free $NaLuF_4:Tb^{3+}$ microscintillators (Fig. S12 in Supporting information). Their excellent radioluminescence properties and excellent compatibility with PMDS polymers suggested that the prepared ligand-free $NaLuF_4:Tb^{3+}$ microscintillators were ideally potential for high-performance X-ray luminescence extension imaging.

We took a further step to measure thermally-stimulated luminescence spectra of $NaLuF_4:Tb^{3+}$ microscintillators and nanoscintillators (Figs. 3a and b). The experimental results indicated that the first thermoluminescence peak of microscintillators was 50 °C higher than that of nanoscintillators at the same excitations, which suggested a deeper depth of calculated trap distribution in the $NaLuF_4:Tb^{3+}$ microscintillators (Figs. 3c and d, Fig. S13 in Supporting information). We performed Monte Carlo simulations to investigate the electron migration from traps into crystal lattices with different particle sizes through comparing proportions of electron final positions in defect states. To estimate the positions of electron migration, we considered that the electrons migrate through the host lattices for one thousand steps of nearest-neighbor random walk (Figs. 3e and f). As anticipated, the proportion of remaining electrons in host lattice after the random walk increased substantially in a microscintillator lattice as contrasted with that in a nanoscintillator lattice (Fig. S14 in Supporting information). Based on experimental and simulation results, we proposed a potential mechanism of the ultralong afterglow in the scintillators under X-ray excitation (Fig. 3g). In a $NaLuF_4$ scintillator, X-ray energy was firstly thermalized by all crystal lattice atoms and primarily absorbed by lutetium atoms due to heavy atom effects. Excitons generated by X-rays recombined immediately, while electrons and holes were captured by hard fluoride sublattice to form Frenkel defects. Displacement distances of separated electrons conformed to normal distribution, forming a series of traps from shallow to deep. Influence of thermal fluctuations made trap electrons slowly return to its original position. High energy barrier of deep traps hardly be satisfied by thermal relaxation at room temperature, allowing ultralong-lived afterglow. Excitation of deep traps required extra energy in the form of either optical or thermal stimulation, releasing trap energy and transferring to Tb^{3+} emitters for radiative recombination.

We further constructed a set of X-ray imaging system consisting of three steps: fabrication of flexible X-ray detector, X-ray imaging storage, and imaging reading (Fig. 4a and Fig. S15a in Supporting information). We first used a blade-coating method to fabricate an X-ray imaging detector by embedded $NaLuF_4:Tb^{3+}$ microscintillators into polydimethylsiloxane (PDMS). Next, a target sample was placed between the X-ray imaging screen and an X-ray source for X-ray imaging storage. After that, the detector was heated on a heating plate to read out the imaging information. Scanning electron microscopy (SEM) image indicated the surface of flexible X-ray detector was crack-free and smooth (Figs. 4b and c), which provided the necessary condition for high quality imaging (Fig. S15b in Supporting information). We investigated the relationship between the thickness and scintillator concentration of the X-ray film layer with respect to the spatial frequency of the X-ray detector (Figs. 4d and e, Fig. S16 in Supporting information). We found that as the thickness of the X-ray detector increased, the spatial frequency decreased, which means that the optimal thickness of the X-ray detector depends on the application requirements. In addition, we found that with the increase of the scintillator concentration, the spatial frequency increased. Fig. 4f depicted the modulation transfer function (MTF) curves which were accessed by the slanted-edge method [34]. The spatial frequency was determined as 24.6 lp/mm at the MTF value of 0.2. We further demonstrated that the exquisite structures of a flexible circuit board, an earphone and a fish were clearly imaged under the radiation (Figs. 4g–i). It

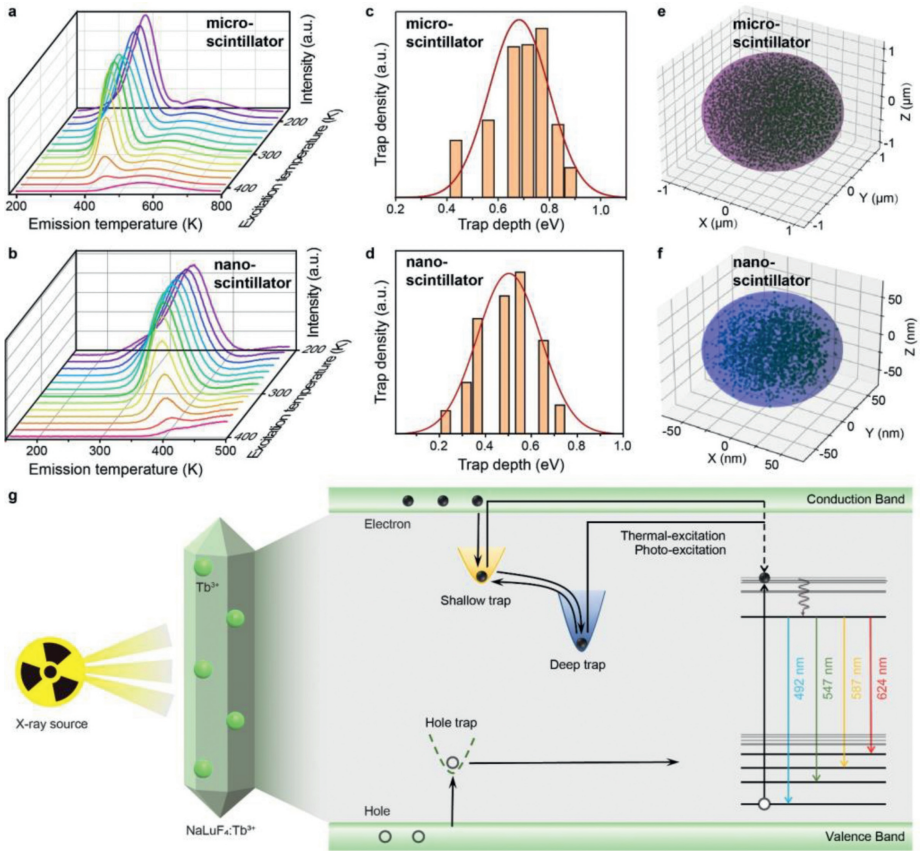

Fig. 3. Mechanistic investigations of lanthanide-doped scintillators. Thermally-stimulated luminescence spectra of $NaLuF_4$:Tb (20 mol%) microscintillators (a) and nanoscintillators (b). The sample was first irradiated by an X-ray source for 300 s. After cessation of the X-ray source for 10 min, emission spectra were measured at a heating rate of 1 K/s. Density distribution of electronic trap depths in lanthanide-doped microscintillators (c) and nanoscintillators (d). The distribution of remaining electrons positions plotted using Monte Carlo simulations for a $NaLuF_4$ microcrystal (e) and a nanocrystal (f). The data sets were constructed by calculating the position of the electron migration after one thousand steps of nearest-neighbor random walk in a cubic crystal lattice. (g) Proposed mechanism of radioluminescence afterglow in Tb^{3+}-doped $NaLuF_4$ scintillators. Upon X-ray excitation, excitons are separated to electrons and holes. Electrons in shallow traps may recombine with holes through conduction band. In contrast, electrons populated in deep traps require additional excitation to be released into Tb^{3+}, where radiative luminescence occurs.

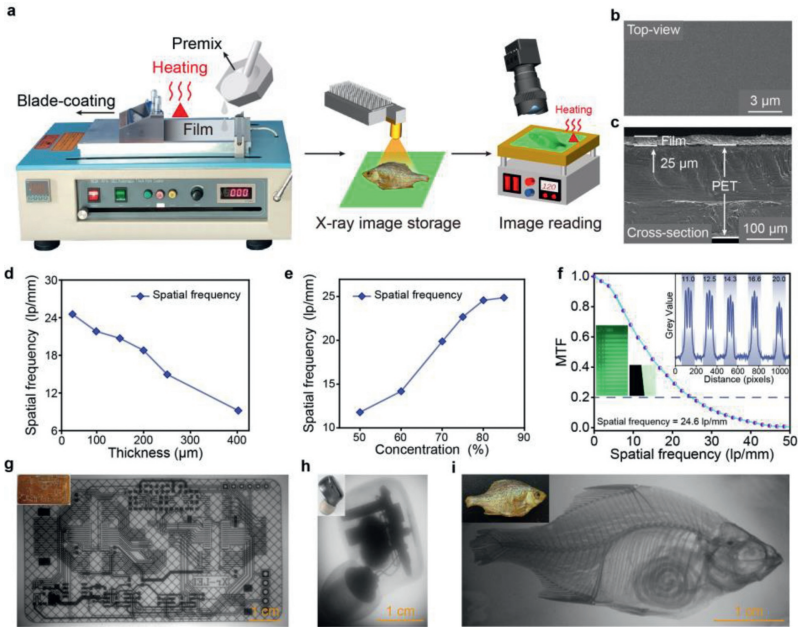

Fig. 4. Fabrication of flexible X-ray detector for digital radiography. (a) Schematic of the experimental setup used for indirect X-ray imaging. The flexible X-ray detector was fabricated by a blade-coating method. A fish was then placed between an X-ray detector and the X-ray source to be imaged. Afterwards, the X-ray detector was placed on a heating plate to readout the imaging information. Top-view (b) and cross-sectional (c) SEM images of an X-ray detector film. The relationship between the thickness (d) and scintillator concentration (e) of the X-ray detector film layer with respect to the spatial frequency of X-ray imaging. (f) Modulation transfer function (MTF) curves of the X-ray imaging. The bottom left inset showed the standard X-ray resolution pattern plate imaging and the X-ray edge image used for MTF calculation. The upper right inset shows the gray value profiles of the line pair. Bright-field and the X-ray images (50 kV, 0.2 mA) of a flexible circuit board (g), an earphone (h), a dried fish (i).

is worth mentioning that all imaging readings were carried out after a month of storage at room temperature after X-ray excitations. Moreover, we also performed X-ray imaging on mice, watch discs, tooth models, USB flash disk, and headfish, showing a wide range of application scenarios (Fig. S17 in Supporting information).

In conclusion, we have developed a concentrated hydrothermal method for the large-scale synthesis of ligand-free lanthanide-doped microscintillators. The obtained high-quality microscintillators exhibited 3 months of ultralong radioluminescence afterglow and 18 months of stability. Through the experimental analysis on the density distribution of electronic trap depths and Monte Carlo simulation results, we found that the deep depth of electron defects induced by X-ray irradiation was reasonable for the long duration of the radioluminescence afterglow. By taking advantage of this ultralong radioluminescence afterglow, we have fabricated a large-area, high-resolution X-ray detector, which has a high X-ray imaging resolution and an excellent X-ray imaging memory. Flexible X-ray detectors made from ligand-free $NaLuF_4:Tb^{3+}$ microscintillators offer a promising application in X-ray luminescence imaging, providing a new option in the field of X-ray information storage.

Declaration of competing interest

The authors declare that they have no known competing financial interests or personal relationships that could have appeared to influence the work reported in this paper.

Acknowledgments

This work is supported by the National Key Research & Development Program of China (Nos. 2020YFA0709900, 2020YFA0210800), the National Natural Science Foundation of China (Nos. 22027805, 62134003, 22104016), the Natural Science Foundation of Fujian Province (Nos. 2022J01709, 2023J01384), and the Major Project of Science and Technology of Fujian Province (No. 2020HZ06006).

Supplementary materials

Supplementary material associated with this article can be found, in the online version, at doi:10.1016/j.cclet.2023.108899.

References

[1] P. Pei, Y. Chen, C. Sun, et al., Nat. Nanotechnol. 16 (2021) 1011–1018.
[2] Z. Hong, Z. Chen, Q. Chen, H. Yang, Acc. Chem. Res. 56 (2023) 37–51.
[3] X. Chen, J. Song, X. Chen, H. Yang, Chem. Soc. Rev. 48 (2019) 3073–3101.
[4] J.H. Heo, D.H. Shin, J.K. Park, et al., Adv. Mater. 30 (2018) 1801743.
[5] W. Zhu, W. Ma, Y. Su, et al., Light Sci. Appl. 9 (2020) 112.
[6] J. Gao, J. Lu, B. Li, et al., Chin. Chem. Lett. 33 (2022) 5132–5136.
[7] Y. He, I. Hadar, M.G. Kanatzidis, Nat. Photon. 16 (2021) 14–26.
[8] B. Zheng, J. Fan, B. Chen, et al., Chem. Rev. 122 (2022) 5519–5603.
[9] K. Cui, P. Li, W. Zhao, et al., Chin. Chem. Lett. 34 (2023) 107797.
[10] G. Blasse, Chem. Mater. 6 (1994) 1465–1475.
[11] H. Chen, J. Chen, M. Li, et al., Sci. Chin. Chem. 65 (2022) 2338–2350.
[12] X. Wang, H. Shi, H. Ma, et al., Nat. Photon. 15 (2021) 187–192.
[13] K. Huang, N. Le, J.S. Wang, et al., Adv. Mater. 34 (2022) 2107962.
[14] Q. Chen, J. Wu, X. Ou, et al., Nature 561 (2018) 88–93.
[15] J. Zhao, L. Zhao, Y. Deng, et al., Nat. Photon. 14 (2020) 612–617.
[16] N. Gan, X. Zou, M. Dong, et al., Nat. Commun. 13 (2022) 3995.
[17] D. Guo, Y. Wang, J. Chen, et al., Chin. Chem. Lett. 34 (2023) 107882.
[18] Y. Liu, Y. Yuzhen, T. Tian, et al., Chin. Chem. Lett. 32 (2021) 3061–3065.
[19] Y.C. Kim, K.H. Kim, D.Y. Son, et al., Nature 550 (2017) 87–91.
[20] D. Zhang, Q. Zhang, B. Ren, et al., Nat. Photon. 16 (2022) 284–290.
[21] J. Perego, I. Villa, A. Pedrini, et al., Nat. Photon. 15 (2021) 393–400.
[22] X. Liu, R. Li, X. Xu, Adv. Mater. 35 (2023) 2206741.
[23] F. Zhang, Y. Zhou, Z. Chen, et al., Adv. Mater. 34 (2022) 2204801.
[24] X. Ou, X. Qin, B. Huang, et al., Nature 590 (2021) 410–415.
[25] W. Wang, L. Sang, W. Kong, et al., Chin. Chem. Lett. 31 (2020) 551–553.
[26] H. Tang, S. Liu, Z. Fang, et al., Adv. Opt. Mater. 10 (2022) 2102836.
[27] R. Gao, M.S. Kodaimati, D. Yan, Chem. Soc. Rev. 50 (2021) 5564–5589.
[28] M. Xu, J. Liu, X. Su, et al., Sci. Chi. Chem. 64 (2021) 2125–2133.
[29] Y. Wang, D. Chen, Y. Zhuang, et al., Adv. Opt. Mater. 9 (2021) 2100624.
[30] H. Chen, Q. Wang, G. Peng, et al., Adv. Opt. Mater. 10 (2022) 2102790.
[31] L. Yang, S. Gai, H. Ding, et al., Adv. Opt. Mater. 11 (2023) 2202382.
[32] Y. Zhang, L. Huang, X. Liu, et al., Angew. Chem. Int. Ed. 55 (2016) 5718–5722.
[33] M.J. Berger, J.H. Hubbell, S.M. Seltzer, et al., XCOM: photon Cross Sections Database, 2013.
[34] E. Samei, M.J. Flynn, D.A. Reimann, Med. Phys. 25 (1998) 102–113.